

University of Wollongong

## Research Online

---

Faculty of Engineering and Information  
Sciences - Papers: Part A

Faculty of Engineering and Information  
Sciences

---

1-1-2015

### Local strain analysis of the tertiary oxide scale formed on a hot-rolled steel strip via EBSD

Xianglong Yu

*University of Wollongong, xly991@uowmail.edu.au*

Zhengyi Jiang

*University of Wollongong, jiang@uow.edu.au*

Jingwei Zhao

*University of Wollongong, jzhao@uow.edu.au*

Dongbin Wei

*University of Wollongong, dwei@uow.edu.au*

Ji Zhou

*Tsinghua University*

*See next page for additional authors*

Follow this and additional works at: <https://ro.uow.edu.au/eispapers>



Part of the [Engineering Commons](#), and the [Science and Technology Studies Commons](#)

---

#### Recommended Citation

Yu, Xianglong; Jiang, Zhengyi; Zhao, Jingwei; Wei, Dongbin; Zhou, Ji; Zhou, Cunlong; and Huang, Qingxue, "Local strain analysis of the tertiary oxide scale formed on a hot-rolled steel strip via EBSD" (2015).

*Faculty of Engineering and Information Sciences - Papers: Part A.* 4611.

<https://ro.uow.edu.au/eispapers/4611>

Research Online is the open access institutional repository for the University of Wollongong. For further information contact the UOW Library: [research-pubs@uow.edu.au](mailto:research-pubs@uow.edu.au)

---

## Local strain analysis of the tertiary oxide scale formed on a hot-rolled steel strip via EBSD

### Abstract

This work presents a fine microstructure and local misorientation study of various oxide phases in the tertiary oxide scale formed on a hot-rolled steel strip via electron back-scattering diffraction (EBSD). Local strain in individual grains of four phases, ferrite ( $\alpha$ -Fe), wustite (FeO), magnetite (Fe<sub>3</sub>O<sub>4</sub>) and hematite ( $\alpha$ -Fe<sub>2</sub>O<sub>3</sub>), has been systematically analysed. The results reveal that Fe<sub>3</sub>O<sub>4</sub> has a lower local strain than  $\alpha$ -Fe<sub>2</sub>O<sub>3</sub>, in particular, on the surface and inner layers of the oxide scale. The multiphase oxides along the cracking or  $\alpha$ -Fe<sub>2</sub>O<sub>3</sub> penetration generally develop a high local misorientation. Localised stain along the cracks demonstrates that the misorientation tends to be strong near grain boundaries. The high fraction of small Fe<sub>3</sub>O<sub>4</sub> grains accumulate at the oxide-substrate interface, which leads to a dramatic increase in the intensity of local stain. This variation is due mainly to the phase transformation among the oxide phases, i.e., the Fe<sub>3</sub>O<sub>4</sub> particles during their nucleation and growth. The combined action of stress relief and re-oxidisation is proposed to explain the formation of Fe<sub>3</sub>O<sub>4</sub> seam at the oxide-steel interface. The present study offers an intriguing insight into the deformation behaviour of the tertiary oxide scale formed on steels, and may help with understanding the stress-aided oxidation effect of metal alloys.

### Keywords

strip, via, ebsd, analysis, tertiary, oxide, scale, formed, hot, local, rolled, strain, steel

### Disciplines

Engineering | Science and Technology Studies

### Publication Details

Yu, X., Jiang, Z., Zhao, J., Wei, D., Zhou, J., Zhou, C. & Huang, Q. (2015). Local strain analysis of the tertiary oxide scale formed on a hot-rolled steel strip via EBSD. *Surface and Coatings Technology*, 277 151-159.

### Authors

Xianglong Yu, Zhengyi Jiang, Jingwei Zhao, Dongbin Wei, Ji Zhou, Cunlong Zhou, and Qingxue Huang

# Local strain analysis of the tertiary oxide scale formed on a hot-rolled steel strip via EBSD

Xianglong Yu <sup>1, 2</sup>, Zhengyi Jiang <sup>1, 4\*</sup>, Jingwei Zhao <sup>1</sup>, Dongbin Wei <sup>1, 3</sup>, Ji Zhou <sup>2</sup>, Cunlong Zhou <sup>4\*</sup>,  
Qingxue Huang <sup>4</sup>

<sup>1</sup> School of Mechanical, Materials and Mechatronic Engineering, University of Wollongong, Wollongong, NSW 2522, Australia

<sup>2</sup> State Key Laboratory of New Ceramics and Fine Processing, School of Materials Science and Engineering, Tsinghua University, Beijing, Beijing 100084, China

<sup>3</sup> School of Electrical, Mechanical and Mechatronic Systems, University of Technology, Sydney, NSW 2007, Australia

<sup>4</sup> Shanxi Provincial Key Laboratory on Metallurgical Device Design and Theory, Taiyuan University of Science and Technology, Taiyuan, Shanxi 030024, China

## Abstract

This work presents a fine microstructure and local misorientation study of various oxide phases in the tertiary oxide scale formed on a hot-rolled steel strip via electron back-scattering diffraction (EBSD). Local strain in individual grains of four phases, ferrite ( $\alpha$ -Fe), wustite (FeO), magnetite (Fe<sub>3</sub>O<sub>4</sub>) and hematite ( $\alpha$ -Fe<sub>2</sub>O<sub>3</sub>), has been systematically analysed. The results reveal that Fe<sub>3</sub>O<sub>4</sub> has a lower local strain than  $\alpha$ -Fe<sub>2</sub>O<sub>3</sub>, in particular, on the surface and inner layers of the oxide scale. The multiphase oxides along the cracking or  $\alpha$ -Fe<sub>2</sub>O<sub>3</sub> penetration generally develop a high local misorientation. Localised stain along the cracks demonstrates that the misorientation tends to be strong near grain boundaries. The high fraction of small Fe<sub>3</sub>O<sub>4</sub> grains accumulate at the oxides-substrate interface, which leads to a dramatic increase in the intensity of local stain. This variation is due mainly to the phase transformation among the oxide phases, i.e., the Fe<sub>3</sub>O<sub>4</sub> particles during their nucleation and growth. The combined action of stress relief and re-oxidisation is

proposed to explain the formation of  $\text{Fe}_3\text{O}_4$  seam at the oxides-steel interface. The present study offers an intriguing insight into the deformation behaviour of the tertiary oxide scale formed on steels, and may help with understanding the stress-aided oxidation effect of metal alloys.

**Keywords:** Local deformation; Misorientation; EBSD; Oxide scale; Steel.

\*Corresponding authors: Tel: 61 2 42214545; Fax: 61 2 42215474; Email: jiang@uow.edu.au (Z.Y. Jiang).

Tel: 86 18635592059; Fax: 86 351 6963332; Email: zcunlong@163.com (C. Zhou).

## 1. Introduction

Metallic oxides (scales) formed on the substrate have posed a serious obstacle to ensuring a defect-free surface of steels during hot rolling [1, 2]. In a conventional production line, these oxide scales can generally be classified as primary, secondary and tertiary scales [3]. The tertiary scale is a particular case generated during the finishing rolling and the subsequent cooling down to ambient temperature [1, 4]. This is because the downstream processing of hot-rolled steel depends greatly on the nature of the tertiary oxide scale.

In most cases, a multi-layered oxide scale formed on a steel at high temperature consists of a thin outer layer of hematite ( $\alpha$ -Fe<sub>2</sub>O<sub>3</sub>), an intermediate layer of magnetite (Fe<sub>3</sub>O<sub>4</sub>), and an inner layer of wustite (Fe<sub>1-x</sub>O, with 1-x ranging from 0.83 to 0.95, to be abbreviated as FeO) just above the steel substrate [5, 6]. By contrast, the tertiary oxide scale at room temperature comprises mainly Fe<sub>3</sub>O<sub>4</sub> and  $\alpha$ -Fe<sub>2</sub>O<sub>3</sub> because the unstable FeO will decompose into Fe<sub>3</sub>O<sub>4</sub> and ferrite ( $\alpha$ -Fe) below the eutectoid temperature of FeO at 570 °C [7, 8]. Nevertheless, the distributions of these oxide phases depend largely on the heat treatment and atmospheric conditions during hot rolling, and the alloying elements in the steel composition [2, 9]. In particular, the precipitation of Fe<sub>3</sub>O<sub>4</sub> usually leads to the formation of a fine-grained Fe<sub>3</sub>O<sub>4</sub> layer at the FeO/steel substrate interface, and is also referred to as the ‘magnetite seam’ [3, 10]. The duplex Fe<sub>3</sub>O<sub>4</sub> layers differ in their microstructure rather than the concentration of oxide phases near the oxides/steel interface. Normally, the upper layer is columnar in microstructure, whereas in the lower layer adjacent to the steel substrate is much finer grained such that the grains tend to be equiaxed [11]. The loss of contact at the oxide/steel interface is almost invariably associated with the fine-grained Fe<sub>3</sub>O<sub>4</sub> layer during hot deformation or continuous cooling. The magnetite seam does not result in growth rates which are greatly different from those of growth by the conventional process, where a classic three-layered oxide scale is formed [3, 11].

The occurrence of  $\text{Fe}_3\text{O}_4$  microstructure is also dependent primarily on the microstructure of the steel substrate, such as orientation, alloying elements, temperature and oxidation time, but its effect on whether a magnetite seam is formed is not clear.

The stress relief in oxide scale could be a potential explanation for the formation of magnetite seam [12]. In this point of view, the internal stress state and plastic deformation of oxide scale play a significant role on the integrity of oxide scale [13, 14], such as magnetite seam bonding to the steel substrate. In general, internal stresses are induced by the growth of oxides, thermal expansion mismatch, and applied forces [15], some of which originate from many different causes. In early studies, the Pilling-Bedworth ratio (PBR) was used to explain the growth stress [16], while the stress relaxation mechanism was also considered in some explorations [17]. Recently, the growth stress evolution in multilayered oxides on pure iron was systematically investigated [10]. The relationships between the type of oxide scale and elastic strain, the thickness and integrity of the oxide scale, were presented in an oxide failure mode map [18]. Some models were proposed to evaluate the residual stress [15, 17], and thereby to predict the integrity of oxide scale formed on steels during hot rolling and cooling processes [18, 19]. Most of these models are based on a parabolic growth law and thermal mismatch without considering the growth stress and rolling forces. Some experiments were designed to examine blistering due to oxide growth stresses during isothermal oxidation [20]. A recent experiment reveals that the presence of  $\alpha$ -Fe precipitates in a  $\text{Fe}_3\text{O}_4$  matrix could lead to a rough interface which would enhance the adherence of oxide scale [21]. In addition, the mechanical properties of oxide scale at temperatures ranging from 650 to 1050 °C can be characterised as brittle, mixed, or ductile, based on its integrity [22]. The conclusions drawn from these elegant previous studies seem to indicate that thin oxide scales behave plastically at high temperatures when the deformation is limited to low reductions [23]. Apart from these, it is believed that the fine-grained magnetite seam near the substrate could be triggered by stress relief in the

oxide layer based on  $\text{Fe}_3\text{O}_4$  creep strain under growth stress at 450 °C [10]. This localised oxidation is related to local stress intensity such as oxide (or oxide and substrate) creep and grain orientation. It is therefore expected to provide a mechanism for cracks propagation resulted from the accumulation of local stress [12]. However, the physical basis for this has not been well established.

In the present study, we aim to evaluate the local strain extracted from the local misorientation in tertiary oxide scale after hot rolling-accelerated cooling (HR-AC) process. Three subsets, namely, the surface, intermediate and inner layers, have been divided to identify the microstructural and misorientation relationships of the transformation among FeO,  $\text{Fe}_3\text{O}_4$  and  $\alpha\text{-Fe}_2\text{O}_3$ . A strain analysis using electron back-scattering diffraction (EBSD) has been conducted to investigate the local misorientation characteristics of different phases ( $\alpha\text{-Fe}$ , FeO,  $\text{Fe}_3\text{O}_4$  and  $\alpha\text{-Fe}_2\text{O}_3$ ) in the divided three subsets. The distribution of local misorientation in these phases and their grain boundary characters have then been used to evaluate the deformation behaviour of the tertiary oxide scale.

## **2. Experimental method**

### **2.1 Material and HR-AC tests**

The material used was a micro-alloyed low-carbon steel for an automotive beam. Its chemical compositions are listed in Table 1. The steel strips were cut into a sheet sample of  $400 \times 100 \times 3$  mm<sup>3</sup>. These samples were then ground to a surface finish of 0.5  $\mu\text{m}$  using SiC papers with 2400 mesh, and cleaned in a solution of acetone prior to HR-AC tests.

HR-AC experiments were performed on a 2-high Hille 100 experimental mill combined with an accelerated cooling system. Full details of the experimental instruments can be found elsewhere [24]. The following procedure was carried out for every HR-AC test. Each sheet was reheated to

900 °C at a rate of 1.7 °C /s under a high purity nitrogen atmosphere, and held for 15 min to ensure a uniform temperature and homogenise the austenite grains. The reheated sheet was then rolled with a thickness reduction of 28% at a rolling speed of 0.3 m/s without any lubrication, followed by an accelerated cooling with a cooling rate of 28 °C/s. Finally, the hot-rolled sheet was air-cooled to obtain the tertiary oxide scale at room temperature. In this case, the temperature at which free cooling commences is 619 °C. This temperature is similar to the coiling temperature in the conventional hot rolling process.

## **2.2 Analytical methodology**

Samples were cut from the centre of the hot-rolled sheet along the rolling direction (RD)–normal direction (ND) plane. In order to fit into the sample holder of the ion milling stage, the samples were sectioned into blocks of dimensions  $20 \times 20 \times 7.8 \text{ mm}^3$  using a Struers Accutum-50 cutting machine. After gold deposition of the samples, the edges for cross sectional analysis were ground using SiC papers with 2000 mesh, and then ion-milled at 6 kV for 5 h using a TIC020 system. Microstructural characterisation was studied using a JEOL JSM 7001F Schottky field emission gun (FEG) scanning electron microscope (SEM) with a Nordlys-II (S) EBSD detector, operated at an acceleration voltage of 15 kV, a probe current of around 2–5 nA, a working distance of 15 mm, and a step size of 0.125  $\mu\text{m}$ .

## **2.3 Analytical procedure**

Post-processing of acquired dataset was carried out using Channel 5 software, where both local misorientation and strain data were extracted from the EBSD maps. The result of kernel average misorientation analysis depends sensitively on the initial noise reduction and the selection criteria

for neighbouring points. In the noise reduction, an angular resolution for the grain reconstruction was maintained at a constant value of  $2^\circ$  in order to reduce orientation noise and retain orientation contrast/texture information. Correspondingly,  $2^\circ \leq \theta < 15^\circ$  misorientations are defined as low-angle grain boundaries (LAGBs), whereas the high-angle grain boundaries (HAGBs) are  $\theta \geq 15^\circ$ . As such, a grain boundary can be classified geometrically in terms of the relative misorientation between the neighboured grains. In phase analysis, a combined EBSD–EDS analysis technique was also used to prevent the misindexing and further improve phase identification [25, 26]. Some other post-processing details can be found in our previous study [25]. The EBSD phase maps were finally divided into four subsets comprising  $\alpha$ -Fe,  $\text{Fe}_3\text{O}_4$ ,  $\text{Fe}_{1-x}\text{O}$  and  $\alpha$ - $\text{Fe}_2\text{O}_3$  for local strain analysis. Orientation distributions of the four subsets were calculated based on the orientations of collected individual grains.

The latter point of local strain analysis is what one selects as the criteria for discarding neighbouring points. Local strain analysis here was constructed using the Kernel average misorientation approach [27]. The local misorientation between the neighbouring pixels within an individual grain was used for representing the local strain caused by the plastic strain [27, 28]. The average misorientation of that point with all of its neighbours is calculated on the condition that misorientations exceeding a tolerance value are excluded from averaging calculation. The tolerance value for the judgment of grain interior is generally equal to  $5^\circ$ . Generally, the predetermined tolerance angle is between  $3$  and  $12.5^\circ$  [29]. The tolerance angle of  $5^\circ$  here was chosen in order to avoid the overlapping of the grain groups in this case, which could be derived from the propagation of some cracks beyond the initiating grains [30]. Since the point-to-point misorientation is often small it is sometimes difficult to discriminate the actual misorientation from the measured orientations, which has an error associated with it of  $0.5$ - $1^\circ$  [31]. Hence, misorientations larger than  $5^\circ$  were regarded as grain boundaries. No overlapping in averaged area was considered. The misorientation for the local strain

evaluation was taken based on the averaged map in this study.

### 3. Results

#### 3.1 Microstructure characterisation

EBSD inverse pole figure (IPF) and grain boundary map in Fig. 1 illustrate a specific grain orientation and microstructure of the oxide sample at a thickness reduction of 28% and a cooling rate of 28 °C/s. Fig. 1b and c show the colour coded for the individual grains in IPF orientation map, displaying their absolute orientations relating to a stereographical triangle. Fig. 1b is for the cubic symmetry material, such as FeO, Fe<sub>3</sub>O<sub>4</sub> and  $\alpha$ -Fe, and Fig. 1c for the trigonal  $\alpha$ -Fe<sub>2</sub>O<sub>3</sub>. In Fig. 1d grain boundary map,  $2^\circ \leq \theta < 15^\circ$  misorientations are defined as LAGBs, whereas, the HAGBs are  $\theta \geq 15^\circ$ . In any case, the intermediate Fe<sub>3</sub>O<sub>4</sub> layer in the IPF and grain boundary maps develops a columnar-shape microstructure between the outer granular grains and the globular inner layer. Indeed, the multi-layered microstructure, i.e. the columnar shape in the upper layer and the refined grains in the lower layer, is the typical Fe<sub>3</sub>O<sub>4</sub> seam as addressed elsewhere [11]. Previous studies [32, 33] have indicated that the granular shape of FeO is elongated along the oxide/steel interface at high temperature, and they are likely to remain intact there after the diffusion of cations and electrons. Therefore, in this case of micro-alloyed low carbon steel, the layered microstructure can be attributed to the decomposition from thermally grown FeO above 570 °C.

EBSD phase map of the deformed sample (Fig. 2a) indicates the distribution of oxide phases formed on the steel substrate. The oxide scale consists of a two-layered microstructure with a thin outer layer of  $\alpha$ -Fe<sub>2</sub>O<sub>3</sub> and an inner duplex Fe<sub>3</sub>O<sub>4</sub> layer. The retained FeO and eutectoid  $\alpha$ -Fe

disperse over the  $\text{Fe}_3\text{O}_4$  matrix.  $\alpha\text{-Fe}_2\text{O}_3$  near the surface gradually penetrates into the cracks within the oxide scale, as shown in Fig. 2a (inset A).

Based on the microstructural examination of oxide scale, it has been possible to identify, in three distinct subsets, the microstructural and local misorientation relationships of oxide phases. The first morphological type is the surface layer that is characterised by a high fraction of trigonal  $\alpha\text{-Fe}_2\text{O}_3$  and a relatively small area fraction of cubic  $\text{Fe}_3\text{O}_4$  or retained FeO constituent (Figs. 2a (inset A) and 3a). The second morphological type comprises a crack in the intermediate layer, where  $\alpha\text{-Fe}_2\text{O}_3$  forms along the crack edges in the  $\text{Fe}_3\text{O}_4$  matrix with scattering retained FeO (Figs. 2a (inset B) and 4a). At the oxides-substrate interface, the fresh steel protrudes into the oxide scale due to different plastic flows of the oxide scale and steel substrate, as shown in (Figs. 2a (inset C) and 5a). This is the third case that the detail analysis performs on.

As seen in Fig. 2b, each pixel in the corresponding local misorientation map is coloured as a function of the average misorientation between the given pixel and all of its neighbours. Misorientation greater than  $5^\circ$  is excluded for this map construction. This is because the definition of grains in EBSD differs from that used in tradition metallography. In EBSD, two neighbouring scan points belong to the same grain if the misorientation between them is less than some value prescribed by a default value. Here the default grain tolerance angle of  $5^\circ$  is enough for our purpose in this relatively low loading test thereby localised deformation. In comparison with EBSD phase map (Fig. 2a), it reveals that the multiphase oxides generally exhibit a higher misorientation. In particular, this large misorientation developed around the cracking concurrently the penetration of  $\alpha\text{-Fe}_2\text{O}_3$  (Fig. 2a (inset B)) or  $\text{Fe}_3\text{O}_4$  (Fig. 2a (inset C)). These regions of high local misorientation are mentioned to be in areas with a fine grain size. Similar results have been given to show us what the grain structure looks like in IPF and grain boundary maps (Fig. 1). Note that a combined EBSD/EDS

analysis technique was also used to prevent the misindexing and further improve phase identification [25, 26]. In doing so, similar crystal structures presented here can be distinguished in particular when there are fine grains. The high fraction of local misorientation occurred in the subsets is probably due to the accumulation of considerable plastic strain and the attendant generation of misfit dislocations in the multiphase oxides [34, 35]. The mechanics could effectively accommodate the substantial dilatational misfit strain associated with the oxidation of  $\text{Fe}^{2+}$  to  $\text{Fe}^{3+}$ .

### 3.2 Distribution of local misorientation in the surface layer of $\alpha\text{-Fe}_2\text{O}_3/\text{Fe}_3\text{O}_4$

Fig. 3 shows the representative local strain analysis of the surface layer from Fig. 2a (inset A). As seen in the EBSD phase map (Fig. 3a) and deformation map of the same location (Fig. 3b) measured as local misorientation, there is a high level of misorientation in mix phases around cracks compared to the pure  $\text{Fe}_3\text{O}_4$  matrix. It is widely believed that heavily deformed areas in the microstructure typically reveal high values of the local misorientation. In addition, Fig. 3c-f indicates the statistical distributions of local misorientation for different phases, together with their regression curves optimised using the log-normal distribution. The probability density function is defined by [27, 28]:

$$f(M_L) = \frac{1}{(\ln S)M_L\sqrt{2\pi}} \exp \left[ -\frac{1}{2} \left( \frac{\ln M_L - \ln M_{ave}}{\ln S} \right)^2 \right] \quad (1)$$

where  $M_L$  and  $S$  are the local misorientation and standard deviation, respectively, and  $M_{ave}$  is the mean value of the distribution which can be calculated by the following equation:

$$M_{ave} = \exp \left[ \frac{1}{N} \sum_{i=1}^N \ln \{M_L(p_i)\} \right] \quad (2)$$

where  $N$  is the number of data. It should be noted that only grains consisting of more than 10 points were included in the calculation; whereas smaller grains were ignored. The local misorientation distribution seems to be well-represented by a lognormal distribution. This was the same for the following figures and other measurements made in this study.

As seen in Fig. 3 c-f, there is a marked difference between different phases in surface layer. The mean local misorientation of  $\text{Fe}_3\text{O}_4$  has a relatively low value ( $M_{ave}=0.45^\circ$ ) compared to that of  $\alpha\text{-Fe}$  ( $M_{ave}=1.07^\circ$ ) and  $\alpha\text{-Fe}_2\text{O}_3$  ( $M_{ave}=0.93^\circ$ ). It implies that the strain energy is rather low during the deformation in the surface layer of  $\text{Fe}_3\text{O}_4$  [36]. This can be verified in Fig. 3g that small grain boundaries occur in  $\alpha\text{-Fe}_2\text{O}_3$  along a straight line a-b in Fig. 3a. The distribution of misorientation angles in cubic crystals has a cutoff at  $62.8^\circ$ , whereas trigonal  $\alpha\text{-Fe}_2\text{O}_3$  has a maximum cutoff at  $95^\circ$  [28]. The distribution of misorientations was inhomogeneous and different grain by grain. Particularly, the misorientation tends to be large near grain boundaries. It is thus clear that the strain energy is easy for the coarse-grained structure to store during the high temperature deformation [36].

### 3.3 Distribution of local misorientation in the intermediate layer of $\text{Fe}_3\text{O}_4$

Representative arrangements of one cracks in the intermediate oxide layer from Fig. 2a (inset B) are shown in Fig. 4. The morphologies shown in Figs. 3a and 4a are the similar  $\alpha\text{-Fe}_2\text{O}_3$  around the crack edges. The misorientation map in Fig. 4b also shows highly localised deformation fields around the cracks. A result that suggests that some of the energy supplied by the cracking could

have been dissipated by plastic work and resulted in misorientation tracked in Fig. 4b. In order to reveal the deformation mechanism, the variations in local misorientation in different phases have been investigated, as shown in Fig. 4 c-f. In analogy to the surface layer, there is a similar trend of the average local misorientation for these four phases in the intermediate oxide layer. The mean local misorientation of  $\text{Fe}_3\text{O}_4$  has a relatively low value ( $M_{\text{ave}}=0.66^\circ$ ) compared to that of  $\alpha\text{-Fe}$  ( $M_{\text{ave}}=0.81^\circ$ ) and  $\alpha\text{-Fe}_2\text{O}_3$  ( $M_{\text{ave}}=1.11^\circ$ ). A possible explanation is that the penetrated  $\alpha\text{-Fe}_2\text{O}_3$  and decomposed  $\alpha\text{-Fe}$  share the relatively small grain size along the cracks. This is because the larger grains suffer from a higher degree of plastic deformation compared to the smaller grains [37]. The misorientation profile along the cracking line (Fig. 4g) further verifies that there are a high fraction of grain boundaries at misorientation angles above  $62.8^\circ$ , which belongs to trigonal  $\alpha\text{-Fe}_2\text{O}_3$ .

### 3.4 Distribution of local misorientation in the oxides-substrate interface layer of $\text{Fe}_3\text{O}_4$

Compared to the outer oxide layers, a noticeable feature in the oxides-substrate interface is free of  $\alpha\text{-Fe}_2\text{O}_3$  phase, as shown in Fig. 5a. Also, the fresh steel protrudes into the oxide scale at a high deformation due to different plastic flows of the oxide scale and steel substrate [38]. Accordingly, the high intensity of local misorientation (Fig. 5b) can also be detected along this oxides-substrate interface. The variation of local misorientation could occur in the  $\text{Fe}_3\text{O}_4$  particles during their nucleation and growth phase. This is also confirmed by previous studies on the formation of the magnetite seam at the oxides-substrate interface [39]. Similarly, the trend of the average local misorientation developed in Fig. 5 c-e is that  $\text{Fe}_3\text{O}_4$  has a minimum value ( $M_{\text{ave}}=0.19^\circ$ ) compared to that of  $\alpha\text{-Fe}$  ( $M_{\text{ave}}=4.18^\circ$ ) and  $\text{FeO}$  ( $M_{\text{ave}}=0.67^\circ$ ). It is noted that the high value of average local misorientation in  $\alpha\text{-Fe}$  may attribute to the disturbance from the steel substrate itself. The pronounced difference is the high fraction small grains accumulated at the oxides-substrate interface. This can be confirmed that the misorientation profile in the oxide layer along the line h-i (Fig. 5a

and f) indicates the relatively sparse grain boundaries and thereby a large grain size here. On the contrary, Fig. 5f reveals that much more grain boundaries occur at the oxide-substrate interface along the line j-k in Fig. 5a. This finding provides an intriguing insight to delineate the formation mechanism of the magnetite seam, whatever the stress relief [10, 12], and further re-oxidisation [11]. Moreover, the characters of these grain boundaries in the magnetite seam may have formed to strains accommodated to this process.

### 3.5 Phase boundary between $\alpha$ -Fe<sub>2</sub>O<sub>3</sub> and Fe<sub>3</sub>O<sub>4</sub>

The use of EBSD allows us to characterise the grain and phase boundaries with respect to their misorientation. A representative orientation relationship across the phase boundaries (between the cubic Fe<sub>3</sub>O<sub>4</sub> and the trigonal  $\alpha$ -Fe<sub>2</sub>O<sub>3</sub>) was obtained on the basis of several EBSD measurements of cross section areas. Fig. 6 illustrates the lattice correlation boundaries between Fe<sub>3</sub>O<sub>4</sub> (Mt) and  $\alpha$ -Fe<sub>2</sub>O<sub>3</sub> (Hm). This relationship corresponds to the matching planes and direction  $\{111\}_{Mt}||\{0001\}_{Hm}$  and  $\{110\}_{Mt}||\{11\bar{2}0\}_{Hm}$  (see grey boundaries in Figs. 3a and 4a). In most cases, these boundaries have a relatively high deviation 3° from the lattice correlation of  $\{111\}_{Mt}||\{0001\}_{Hm}$ . The same case occurs in the lattice correlation of  $\{110\}_{Mt}||\{11\bar{2}0\}_{Hm}$ . Although large angle deviation may be described from both lattice correlations up to 55° to  $\{111\}_{Mt}||\{0001\}_{Hm}$  and up to 30° to  $\{110\}_{Mt}||\{11\bar{2}0\}_{Hm}$ , the most frequent deviation angle of the correlation  $\{111\}_{Mt}||\{0001\}_{Hm}$  is not above 5°, delimited by the dashed line in the Fig. 6. In regard to the correlation  $\{110\}_{Mt}||\{11\bar{2}0\}_{Hm}$ , the high frequency ranges 28-30° (in Fig. 6). Nevertheless, the favoured basal slip, i.e., aligning  $\{0001\}$  planes, normally dominates in trigonal  $\alpha$ -Fe<sub>2</sub>O<sub>3</sub> [28]. Similarly, it is believed that the correlation  $\{111\}_{Mt}||\{0001\}_{Hm}$  also plays the major role in the analysis of phase boundaries. In any case, two direct evidences here can be responsible for oxidation as the main process responsible for the growth of new grains of interior  $\alpha$ -Fe<sub>2</sub>O<sub>3</sub>: 1) the

coincidence of the orientation of the planes  $\{111\}\{0001\}$  and  $\{110\}\{11\bar{2}0\}$ , 2) the presence of the boundaries of low angle with specified lattice correlation of  $\{111\}_{\text{Mt}}\|\{0001\}_{\text{Hm}}$  and  $\{110\}_{\text{Mt}}\|\{11\bar{2}0\}_{\text{Hm}}$ . Therefore, the  $\alpha\text{-Fe}_2\text{O}_3$  crystals inside the  $\text{Fe}_3\text{O}_4$  are the result of a direct transformation process. Thereby, the influence of phase boundaries between  $\text{Fe}_3\text{O}_4$  and  $\alpha\text{-Fe}_2\text{O}_3$  on misorientation will be discussed next.

#### 4. Discussion

Given the fact that the distributions of normalised plastic strain do not change significantly with the level of macroscopic strain, it means that it is sufficient to focus on one level of macroscopic plastic strain for further analysis [40]. Due to the local misorientation correlated with the fine step size as well as the magnitude of the macroscopic plastic strain, the relationship between these parameters can be used to estimate the degree of the local plastic strain [37, 39]. Fig. 7 shows the relationship between the nominal plastic strain,  $\varepsilon_p$ , and the averaged local misorientation for a fine step size of  $0.125\ \mu\text{m}$  in this study. The averaged local misorientation for unstrained conditions is set to  $M_{\text{ave}}=0.1$ . For the estimation of local plastic strain, a linear regression of the data above 10% plastic strain can be modified as [37]:

$$\varepsilon_p = \frac{M_L - 0.1}{-0.0027d^2 + 0.0041d} \quad (3)$$

where the strain is given in percent and step size  $d$ . In this study, the step size is set as  $0.125\ \mu\text{m}$ .

As seen in Fig. 7, the local plastic strain varies drastically in various oxide phases.  $\text{Fe}_3\text{O}_4$  has the relatively low values of plastic strain below 7.2%, where a high value occurs in the surface layer of the oxide scale. It suggests that there is rather low strain energy during the deformation in the  $\text{Fe}_3\text{O}_4$

layer compared to the  $\alpha$ -Fe<sub>2</sub>O<sub>3</sub> layer and steel substrate. This is because the stress relief caused by some cracking of oxide scale could occur during the high temperature deformation, thereby lead to the different misorientation distributions in magnetite seam. This left less energy available for cracks growth, the oxidation of  $\alpha$ -Fe<sub>2</sub>O<sub>3</sub> or decomposition of FeO.

Nevertheless, note that the aim of the present study has been to clarify the magnitude and the origins of plastic strain heterogeneity in the tertiary oxide scale deformed under conditions where multi-phases dominates. Finding a correlation between local misorientation and macroscopic plastic strain is one thing to achieve this. While the origins of the local misorientations can be due to plastic strain, local plastic strain is not simply correlated to macroscopic plastic strain, particularly for anisotropic materials Fe<sub>3</sub>O<sub>4</sub> and  $\alpha$ -Fe<sub>2</sub>O<sub>3</sub> here. That means that the estimated plastic strain does not correspond to the nominal plastic strain [27]. This is because the local misorientation correlates with the geometrically necessary dislocations rather than the magnitude of deformation. The estimated local plastic strain just shows the typical local misorientation that is observed under the plastic strain. Therefore, the local plastic strain is determined not only by applied plastic strain but also by geometry of grain structure [41, 42], crystal orientation [23, 43].

As it is the case for the plastic strain presented here, the second thing is possible that the spatial heterogeneity of the plastic strain amplitude is linked to the underlying crystallographic orientation of the grain and also grain size. In Figs. 3b and 4b, localised plasticity that is initiated in small cracks near  $\alpha$ -Fe<sub>2</sub>O<sub>3</sub> grains spreads in the form of narrow strain bands throughout the oxide scale. Moreover, those regions where significant local heterogeneities in  $\alpha$ -Fe<sub>2</sub>O<sub>3</sub> distribution govern show the strain heterogeneity. The variation in crystallographic orientations at oxide/steel interface (Fig. 1) also suggests that the effect of crystallographic orientation could be more dominant than the effect of grain size for the initiation of plasticity in this case. It is noted that trigonal  $\alpha$ -Fe<sub>2</sub>O<sub>3</sub> rather than

cubic  $\text{Fe}_3\text{O}_4$  is strongly anisotropic and involves different microscopic mechanisms such as mechanical twinning and dislocation glide [44, 45]. Thus, the mismatch between  $\alpha\text{-Fe}_2\text{O}_3$  and  $\text{Fe}_3\text{O}_4$  are often considered to be responsible for various peculiar features of plastic flow [46]. However, previous study [29, 44] reveals that intragranular plastic strain heterogeneity have revealed plastic strains as large as 5 times the macroscopic tensile strain. Large local strains were found to be statistically linked to proximity to grain boundaries. This infers the importance of interactions between neighbouring grains. Thus, it can be expected that local strains can be influenced by phase boundaries in oxide scale, as the processes at each individual boundary are controlled by its properties.

In addition, our results reveal that the phase relationships between  $\text{Fe}_3\text{O}_4$  and  $\alpha\text{-Fe}_2\text{O}_3$  is  $\{111\}_{\text{Mt}}\|\{0001\}_{\text{Hm}}$  and  $\{110\}_{\text{Mt}}\|\{11\bar{2}0\}_{\text{Hm}}$  in presence of low angle boundaries (Fig. 6). This infers that the growth of new  $\alpha\text{-Fe}_2\text{O}_3$  grains occurs in the vicinity of the grain boundaries in the  $\text{Fe}_3\text{O}_4$  grains. It is well known that in dual-phase steels a higher  $\alpha\text{-Fe}$  fraction experiences local plastic deformation due to the martensitic phase transformation [47]. Similarly, the certain local plastic deformation in tertiary oxide scale could occur due to phase transformation among oxide phases. More importantly, the local misorientation map (Fig. 2) illustrates considerable orientation gradients spreading from the  $\text{Fe}_3\text{O}_4\text{-}\alpha\text{-Fe}_2\text{O}_3$  phase boundaries into the  $\text{Fe}_3\text{O}_4$  grain interior. Thus, the local misorientation can influence crack propagation or initiation in oxide scale. As such, the plastic strain assessment and strain quantity within individual grains are essential for understanding the material susceptibility to cracks at various loading conditions and heat treatments [48]. Since the spatial distribution of plastic strain has been quantified at the microstructural scale for the tertiary oxide scale, we are still under the way to understand the local strain behaviour in cubic  $\text{Fe}_3\text{O}_4$  and trigonal  $\alpha\text{-Fe}_2\text{O}_3$ . Our results provide a deep insight to understand the nature of defects and their distribution within the tertiary oxide scale, thereby to control the formation of oxide scale during

steel processing at high temperature.

## 5. Conclusion

Local strain/misorientation evolution of four phases ( $\alpha$ -Fe, FeO, Fe<sub>3</sub>O<sub>4</sub> and  $\alpha$ -Fe<sub>2</sub>O<sub>3</sub>) in tertiary oxide scale formed on a Nb-V-Ti steel subjected to a thickness reduction of 28% and cooling rate of 28 °C/s have been quantitatively characterised via EBSD, and systematically analysed. The following conclusions can be drawn.

- (1) The regions with the multiphase oxides in the tertiary, particularly along the cracking edges and the penetration of  $\alpha$ -Fe<sub>2</sub>O<sub>3</sub>, generally develop a relatively high local misorientation.
- (2) Distribution of local misorientation in surface layer of oxide scale reveals that Fe<sub>3</sub>O<sub>4</sub> has a relatively low local strain compared to  $\alpha$ -Fe<sub>2</sub>O<sub>3</sub>. The misorientation tends to be large near grain boundaries.
- (3) The deformation behaviour in the intermediate oxide layer demonstrates that the large grains suffer from a high degree of plastic deformation compared to the small grains. Localised stain fields can be identified in the penetrated  $\alpha$ -Fe<sub>2</sub>O<sub>3</sub> and decomposed  $\alpha$ -Fe along the cracking lines.
- (4) The high fraction of small Fe<sub>3</sub>O<sub>4</sub> grains accumulate at the oxides-substrate interface. This leads to a dramatic increase in the intensity of local stain. The variation of local misorientation is due to the Fe<sub>3</sub>O<sub>4</sub> particles during their nucleation and growth.
- (5) Fe<sub>3</sub>O<sub>4</sub> has the relatively low values of plastic strain below 7.2%. The stress relief caused by

some cracking of oxide scale could occur during the high temperature deformation, and lead to the different misorientation distributions in magnetite seam. The understanding we have gained as to how the local misorientation and grain boundaries take place could aid in the choice and design of the tertiary oxide scale available during hot strip rolling.

## **Acknowledgements**

We are grateful to J. Abbott, L. Hao and S. Rodd for their assistance in the HR-AC experiments. We would like extend special thanks to Dr. Madeleine Cincotta for English language editing. The authors also acknowledge use of facilities within the UOW Electron Microscopy Centre.

## **References**

- [1] D.J. Young, *High Temperature Oxidation and Corrosion of Metals*, Elsevier, Oxford, 2008.
- [2] M. Krzyzanowski, J.H. Beynon, D.C. Farrugia, *Oxide Scale Behavior in High Temperature Metal Processing*, Wiley-VCH, Weinheim, 2010.
- [3] R.Y. Chen, W.Y.D. Yuen, Review of the high-temperature oxidation of iron and carbon steels in air or oxygen, *Oxid. Met.* 59 (2003) 433–468.
- [4] X.L. Yu, Z.Y. Jiang, X.D. Wang, D.B. Wei, Q. Yang, Effect of coiling temperature on oxide scale of hot-rolled strip, *Adv. Mater. Res.* 415–417 (2012) 853–858.
- [5] N. Birks, G.H. Meier, F.S. Pettit, *Introduction to the High-temperature Oxidation of Metals*, 2nd ed., C.U. Press, UK, 2006.
- [6] X.L. Yu, Z.Y. Jiang, J.W. Zhao, D.B. Wei, C.L. Zhou, Q.X. Huang, Effect of a grain-refined microalloyed steel substrate on the formation mechanism of a tight oxide scale, *Corros. Sci.* 85 (2014) 115–125.

- [7] H.A. Wriedt, Fe-O (iron-oxygen), in Massalski, T. B. (Ed.), *Binary Alloy Phase Diagrams*, ASM, Materials Park, 1990, pp. 1739.
- [8] S. Hayashi, K. Mizumoto, S. Yoneda, Y. Kondo, H. Tanei, S. Ukai, The Mechanism of phase transformation in thermally-grown FeO scale formed on pure-Fe in air, *Oxid. Met.* 81 (2014) 357–371.
- [9] X.W. Cheng, Z.Y. Jiang, D.B. Wei, J.W. Zhao, B.J. Monaghan, R.J. Longbottom, L.Z. Jiang, Characteristics of oxide scale formed on ferritic stainless steels in simulated reheating atmosphere, *Surf. Coat. Technol.* 258 (2014) 257–267.
- [10] C. Juricic, H. Pinto, D. Cardinali, M. Klaus, C. Genzel, A.R. Pyzalla, Effect of substrate grain size on the growth, texture and internal stresses of iron oxide scales forming at 450 °C, *Oxid. Met.* 73 (2010) 15–41.
- [11] A. Atkinson, Transport processes during the growth of oxide films at elevated temperature, *Rev. Mod. Phys.* 57 (1985) 437–470.
- [12] H.E. Evans, H.Y. Li, P. Bowen, A mechanism for stress-aided grain boundary oxidation ahead of cracks, *Scripta Mater.* 69 (2013) 179–182.
- [13] J.A. Nychka, C. Pullen, M.Y. He, D.R. Clarke, Surface oxide cracking associated with oxidation-induced grain boundary sliding in the underlying alloy, *Acta Mater.* 52 (2004) 1097–1105.
- [14] G.C. Wood, J. Stringer, The adhesion of growing oxide scales to the substrate, *J. Phys. IV* 3 (1993) 65–74.
- [15] B. Panicaud, J.L. Grosseau-Poussard, J.F. Dinhut, Comparison of growth stress measurements with modelling in thin iron oxide films, *Appl. Surf. Sci.* 252 (2006) 5700–5713.
- [16] M. Schütze, *Protective Oxide Scales and Their Breakdown*, John Wiley & sons, Chichester, 1997.
- [17] S.J. Bull, Modeling of residual stress in oxide scales, *Oxid. Met.* 49 (1998) 1–17.
- [18] M. Torres, R. Colás, Growth and breakage of the oxide layer during hot rolling of low carbon

steels, in Proceedings 1st Int. Conf. Modelling of metal rolling processes, London, 1993, pp. 629–636.

[19]R. Bhattacharya, G. Jha, S. Kundu, R. Shankar, N. Gope, Influence of cooling rate on the structure and formation of oxide scale in low carbon steel wire rods during hot rolling, *Surf. Coat. Technol.* 201 (2006) 526–532.

[20]F. Matsuno, Blistering and hydraulic removal of scale films of rimmed steel at high temperature, *ISIJ Int.* 20 (1980) 413–421.

[21]P.H. Bolt, Understanding the properties of oxide scales on hot rolled steel strip, *Steel Res. Int.* 75 (2004) 399–404.

[22]L. Suárez, Y. Houbaert, X.V. Eynde, R. Colás, High temperature deformation of oxide scale, *Corros. Sci.* 51 (2009) 309–315.

[23]X.L. Yu, Z.Y. Jiang, J.W. Zhao, D.B. Wei, J. Zhou, C.L. Zhou, Q.X. Huang, Dependence of texture development on the grain size of tertiary oxide scales formed on a microalloyed steel, *Surf. Coat. Technol.* 272 (2015) 39–49.

[24]Z.Y. Jiang, X.L. Yu, J.W. Zhao, C.L. Zhou, Q.X. Huang, G.Z. Luo, K.Z. Linghu, Tribological analysis of oxide scales during cooling process of rolled microalloyed steel, *Adv. Mater. Res.* 1017 (2014) 435–440.

[25]X.L. Yu, Z.Y. Jiang, J.W. Zhao, D.B. Wei, C.L. Zhou, Q.X. Huang, Microstructure and microtexture evolutions of deformed oxide layers on a hot-rolled microalloyed steel, *Corros. Sci.* 90 (2015) 140–152.

[26]J.H. Kim, D.I. Kim, J.H. Shim, K.W. Yi, Investigation into the high temperature oxidation of Cu-bearing austenitic stainless steel using simultaneous electron backscatter diffraction-energy dispersive spectroscopy analysis, *Corros. Sci.* 77 (2013) 397–402.

[27]M. Kamaya, Measurement of local plastic strain distribution of stainless steel by electron backscatter diffraction, *Mater. Charact.* 60 (2009) 125–132.

- [28]O. Engler, V. Randle, Introduction to Texture Analysis: Macrotecture, Microtexture, and Orientation Mapping, CRC press, Boca Raton, 2010.
- [29]J.Y. Kang, B. Bacroix, H. Réglé, K.H. Oh, H.C. Lee, Effect of deformation mode and grain orientation on misorientation development in a body-centered cubic steel, *Acta Mater.* 55 (2007) 4935–4946.
- [30]J. Miao, T.M. Pollock, J.W. Jones, Microstructural extremes and the transition from fatigue crack initiation to small crack growth in a polycrystalline nickel-base superalloy, *Acta Mater.* 60 (2012) 2840–2854.
- [31]S.I. Wright, M.M. Nowell, D.P. Field, A review of strain analysis using electron backscatter diffraction, *Microsc. Microanal.* 17 (2011) 316–329.
- [32]R.L. Higginson, B. Roebuck, E.J. Palmiere, Texture development in oxide scales on steel substrates, *Scripta Mater.* 47 (2002) 337–342.
- [33]B.K. Kim, J.A. Szpunar, Orientation imaging microscopy in research on high temperature oxidation, in Schwartz, A. J. (Ed.) *Electron Backscatter Diffraction in Materials Science*, Springer, New York, 2009, pp. 361–393.
- [34]J. Cao, J. Wu, Strain effects in low-dimensional transition metal oxides, *Mater. Sci. Eng. R-Rep.* 71 (2011) 35–52.
- [35]C.P. Chang, M.W. Chu, H.T. Jeng, S.L. Cheng, J.G. Lin, J.R. Yang, C.H. Chen, Condensation of two-dimensional oxide-interfacial charges into one-dimensional electron chains by the misfit-dislocation strain field, *Nat. Commun.* 5 (2014) 3522.
- [36]Y. Takayama, J.A. Szpunar, H. Kato, Analysis of intragranular misorientation related to deformation in an Al-Mg-Mn alloy, *Mater. Sci. Forum* 495 (2005) 1049–1054.
- [37]F. Law, Y. Yi, P.I. Widenborg, J. Luther, B. Hoex, Identification of geometrically necessary dislocations in solid phase crystallized poly-Si, *J. Appl. Phys.* 114 (2013) 043511–5.

- [38]W.J. Cheng, Y.Y. Chang, C.J. Wang, Observation of high-temperature phase transformation in the aluminide Cr–Mo steel using EBSD, *Surf. Coat. Technol.* 203 (2008) 401–406.
- [39]J. Tang, A.K. Tieu, Z.Y. Jiang, Modelling of oxide scale surface roughness in hot metal forming, *J. Mater. Process. Technol.* 177 (2006) 126–129.
- [40]H. Ghadbeigi, C. Pinna, S. Celotto, J.R. Yates, Local plastic strain evolution in a high strength dual-phase steel, *Mater. Sci. Eng. A* 527 (2010) 5026–5032.
- [41]K. Shinoda, M. Demura, H. Murakami, S. Kuroda, S. Sampath, Characterization of crystallographic texture in plasma-sprayed splats by electron-backscattered diffraction, *Surf. Coat. Technol.* 204 (2010) 3614–3618.
- [42]E.M. Lehockey, A.M. Brennenstuhl, I. Thompson, On the relationship between grain boundary connectivity, coincident site lattice boundaries, and intergranular stress corrosion cracking, *Corros. Sci.* 46 (2004) 2383–2404.
- [43]P. Brito, H. Pinto, C. Genzel, M. Klaus, A. Kaysser-Pyzalla, Epitaxial stress and texture in thin oxide layers grown on Fe–Al alloys, *Acta Mater.* 60 (2012) 1230–1237.
- [44]G. Martin, C.W. Sinclair, R.A. Lebensohn, Microscale plastic strain heterogeneity in slip dominated deformation of magnesium alloy containing rare earth, *Mater. Sci. Eng. A* 603 (2014) 37–51.
- [45]C.C. Tasan, J.P. Hoefnagels, M. Diehl, D. Yan, F. Roters, D. Raabe, Strain localization and damage in dual phase steels investigated by coupled in-situ deformation experiments and crystal plasticity simulations, *Int. J. Plasticity* 63 (2014) 198–210.
- [46]L. Suárez, P. Rodríguez-Calvillo, Y. Houbaert, N.F. Garza-Montes-de-Oca, R. Colás, Analysis of deformed oxide layers grown on steel, *Oxid. Met.* 75 (2011) 281–295.
- [47]S. Biroasca, F. Di Gioacchino, S. Stekovic, M. Hardy, A quantitative approach to studying the effect of local texture and heterogeneous plastic strain on the deformation micromechanism in RR1000 nickel-based superalloy, *Acta Mater.* 74 (2014) 110–124.

[48]F. Di Gioacchino, J.Q. da Fonseca, Plastic strain mapping with sub-micron resolution using digital image correlation, *Exp. Mech.* 53 (2013) 743–754.

## List of Figures captions

**Fig. 1** EBSD (a) inverse pole figure (IPF) orientation map, and (d) grain boundary map of the oxidised sample at a thickness reduction of 28% and a cooling rate of 28 °C/s; a colour key for the (b) cubic symmetry  $\alpha$ -Fe, FeO, and Fe<sub>3</sub>O<sub>4</sub>, (c) trigonal  $\alpha$ -Fe<sub>2</sub>O<sub>3</sub>.

**Fig. 2** EBSD (a) phase map for  $\alpha$ -Fe, FeO, Fe<sub>3</sub>O<sub>4</sub> and  $\alpha$ -Fe<sub>2</sub>O<sub>3</sub>; (b) local misorientation map, of the sample; and insets (A) surface, (B) intermediate, (C) oxides-substrate interface, layer.

**Fig. 3** A zoom-in view of the EBSD (a) phase map, (b) local misorientation map of surface layer, inset A in Fig. 2; corresponding to the distribution of local misorientation in the (c)  $\alpha$ -Fe, (d) FeO, (e) Fe<sub>3</sub>O<sub>4</sub>, (f)  $\alpha$ -Fe<sub>2</sub>O<sub>3</sub>; (g) misorientation distribution along the line a-b in Fig. 3a.

**Fig. 4** A zoom-in view of the EBSD (a) phase map, (b) local misorientation map of intermediate layer, inset B in Fig. 2; corresponding to the distribution of local misorientation in the (c)  $\alpha$ -Fe, (d) FeO, (e) Fe<sub>3</sub>O<sub>4</sub>, (f)  $\alpha$ -Fe<sub>2</sub>O<sub>3</sub>; (g) misorientation distribution along the line c-d in Fig. 4a.

**Fig. 5** A zoom-in view of the EBSD (a) phase map, (b) local misorientation map of oxides-substrate interface layer, inset C in Fig. 2; corresponding to the distribution of local misorientation in the (c)  $\alpha$ -Fe, (d) FeO, (e) Fe<sub>3</sub>O<sub>4</sub>; misorientation distribution along the (f) line h-i, and (g) line j-k, in Fig. 5a.

**Fig. 6** Histogram of the lattice correlation boundaries between [110] of Fe<sub>3</sub>O<sub>4</sub> and  $[11\bar{2}0]$  of  $\alpha$ -Fe<sub>2</sub>O<sub>3</sub>, and [111] of Fe<sub>3</sub>O<sub>4</sub> and [0001] of  $\alpha$ -Fe<sub>2</sub>O<sub>3</sub>.

**Fig. 7** Relationship between averaged local misorientation  $M_{ave}$  and macroscopic plastic strain in tertiary oxide scale with different phases.

**Table 1** Chemical compositions of the studied steel.

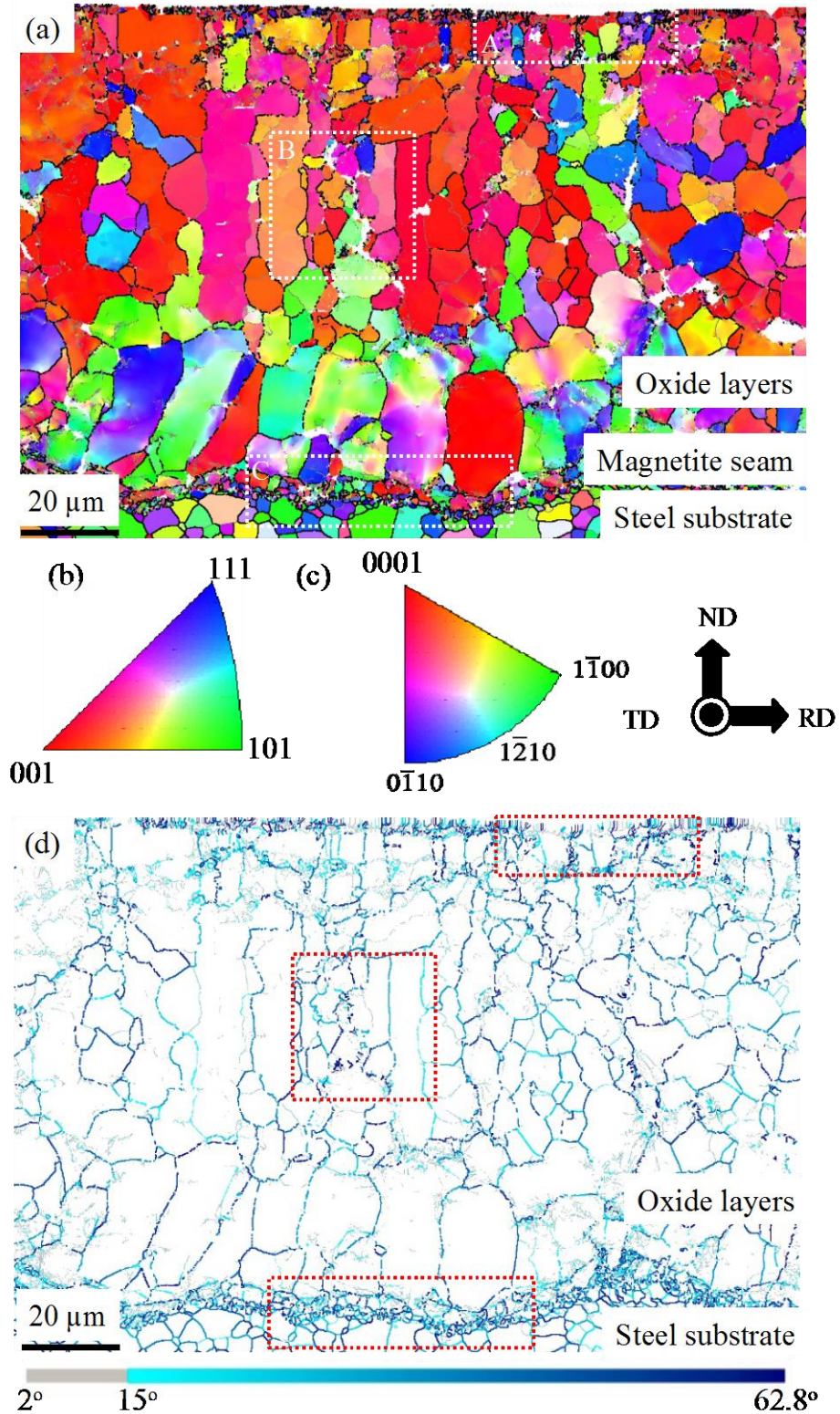


**Fig. 1** EBSD (a) inverse pole figure (IPF) orientation map, and (d) grain boundary map of the oxidised sample at a thickness reduction of 28% and a cooling rate of 28  $^{\circ}\text{C/s}$ ; a colour key for the (b) cubic symmetry  $\alpha\text{-Fe}$ ,  $\text{FeO}$ , and  $\text{Fe}_3\text{O}_4$ , (c) trigonal  $\alpha\text{-Fe}_2\text{O}_3$ .

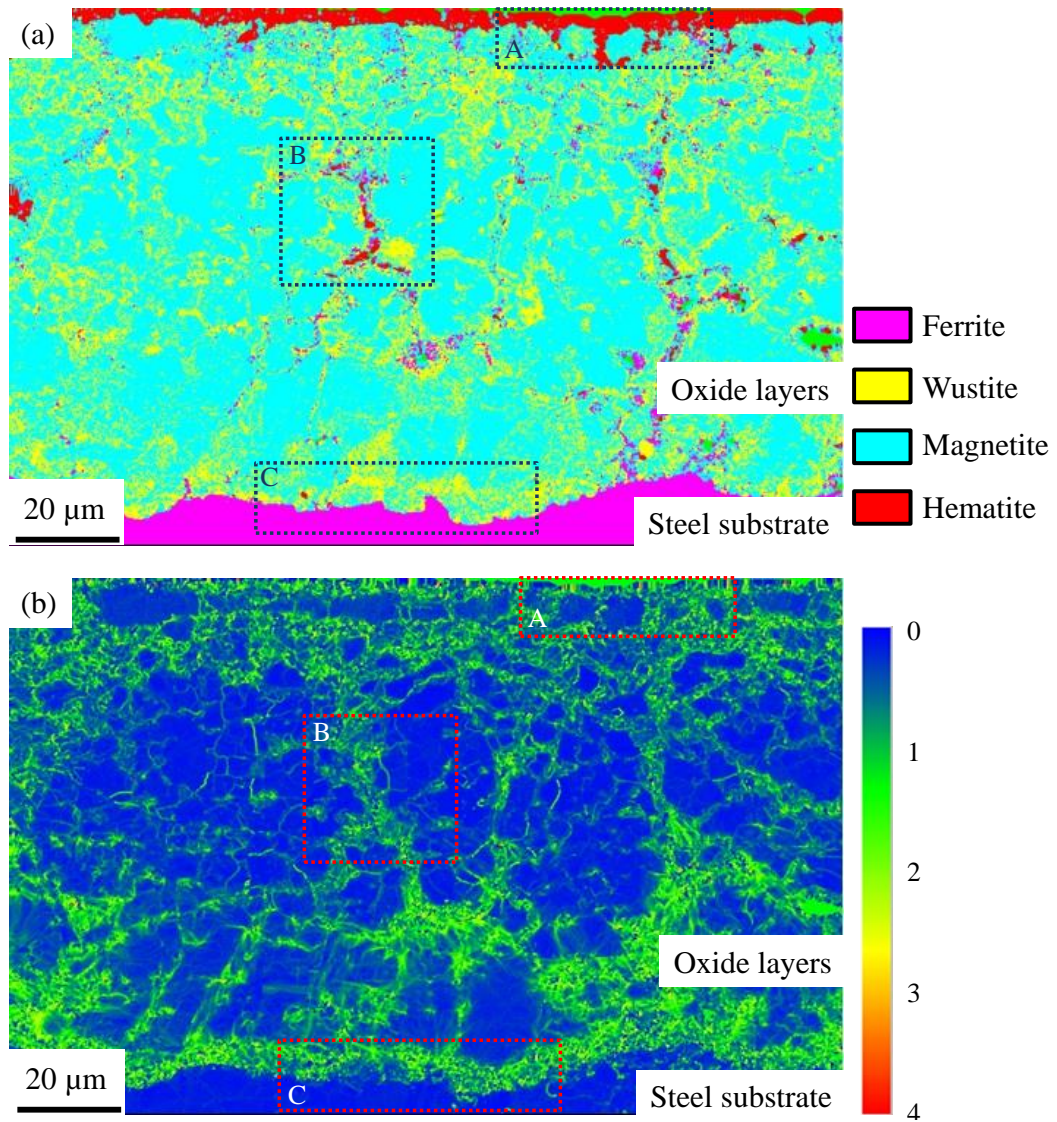


**Fig. 2** EBSD (a) phase map for  $\alpha$ -Fe, FeO, Fe<sub>3</sub>O<sub>4</sub> and  $\alpha$ -Fe<sub>2</sub>O<sub>3</sub>; (b) local misorientation map, of the sample; and insets (A) surface, (B) intermediate, (C) oxides-substrate interface, layer.

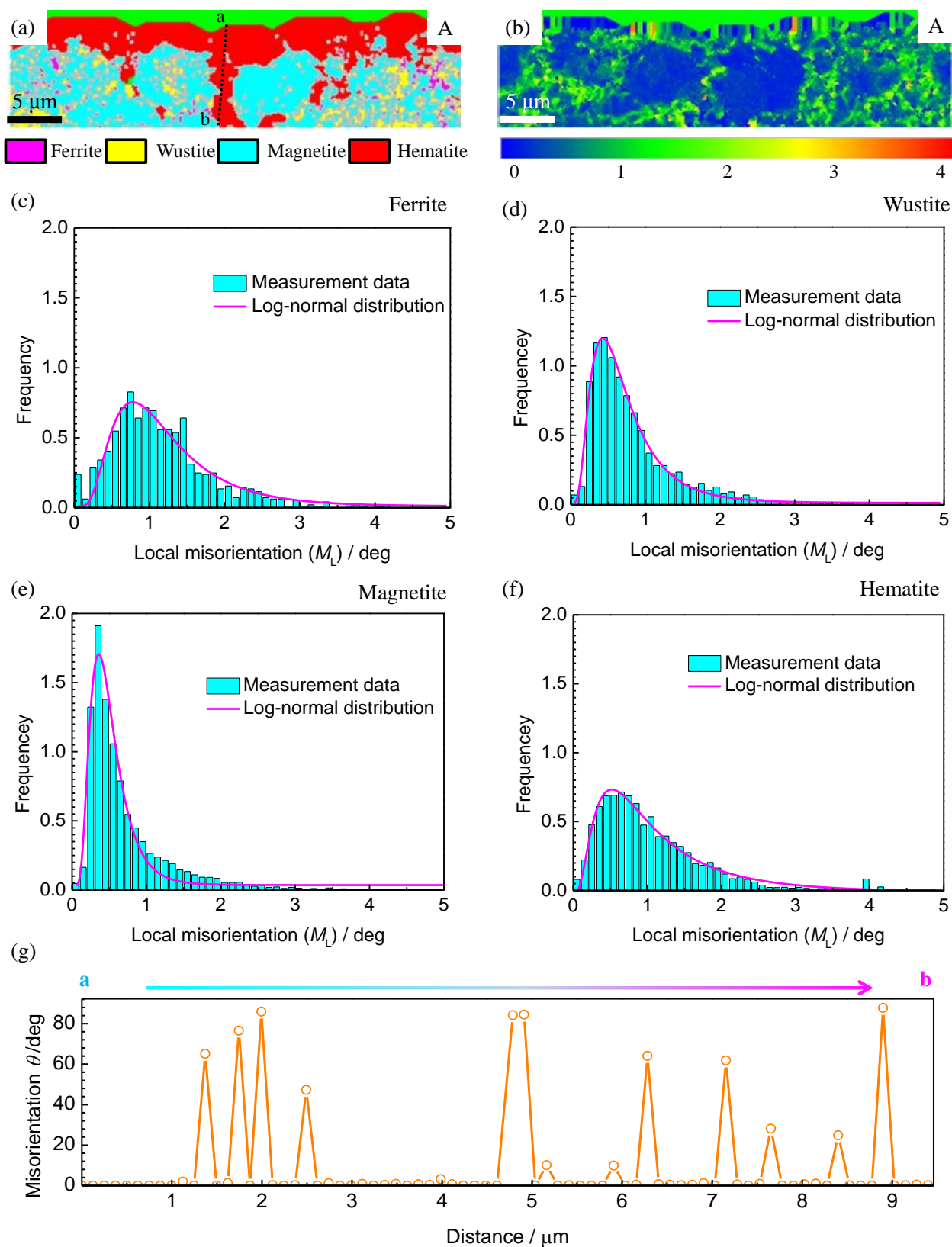


**Fig. 3** A zoom-in view of the EBSD (a) phase map, (b) local misorientation map of surface layer, inset A in Fig. 2; corresponding to the distribution of local misorientation in the (c)  $\alpha$ -Fe, (d) FeO, (e) Fe<sub>3</sub>O<sub>4</sub>, (f)  $\alpha$ -Fe<sub>2</sub>O<sub>3</sub>; (g) misorientation distribution along the line a-b in Fig. 3a.

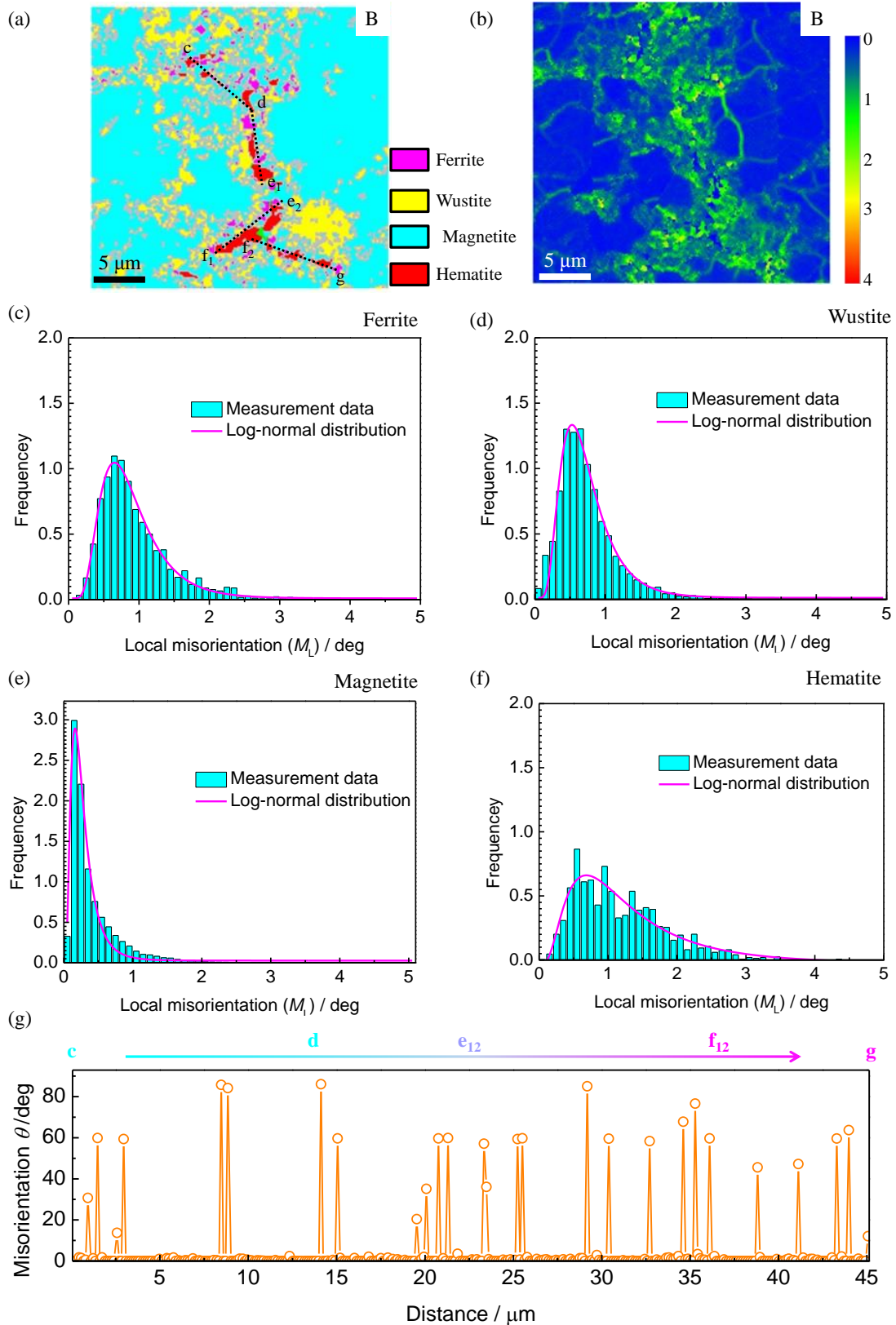


**Fig. 4** A zoom-in view of the EBSD (a) phase map, (b) local misorientation map of intermediate layer, inset B in Fig. 2; corresponding to the distribution of local misorientation in the (c)  $\alpha$ -Fe, (d) FeO, (e)  $\text{Fe}_3\text{O}_4$ , (f)  $\alpha$ - $\text{Fe}_2\text{O}_3$ ; (g) misorientation distribution along the line c-d in Fig. 4a.

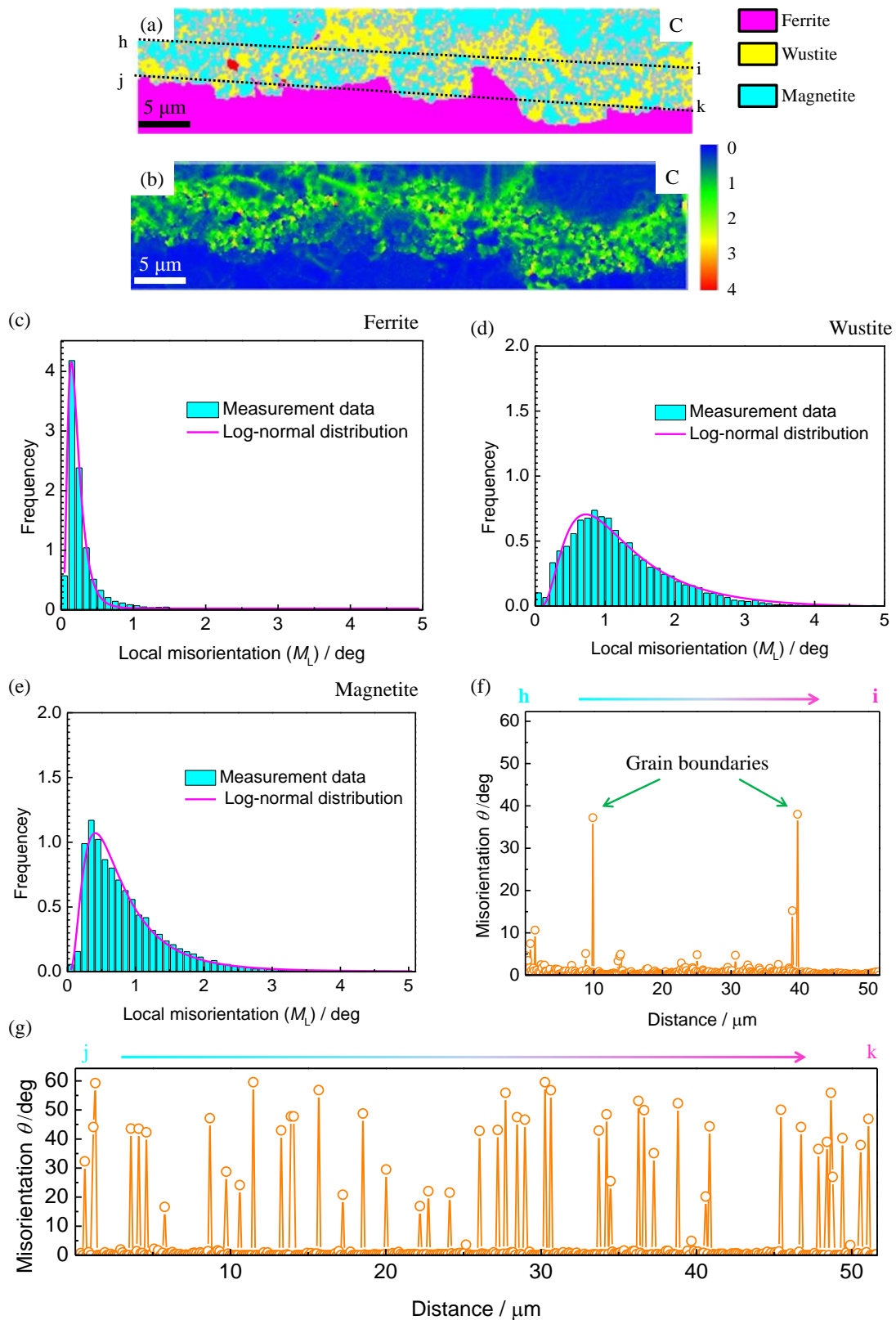


**Fig. 5** A zoom-in view of the EBSD (a) phase map, (b) local misorientation map of oxides-substrate interface layer, inset C in Fig. 2; corresponding to the distribution of local misorientation in the (c)

$\alpha$ -Fe, (d) FeO, (e) Fe<sub>3</sub>O<sub>4</sub>; misorientation distribution along the (f) line h-i, and (g) line j-k, in Fig. 5a.

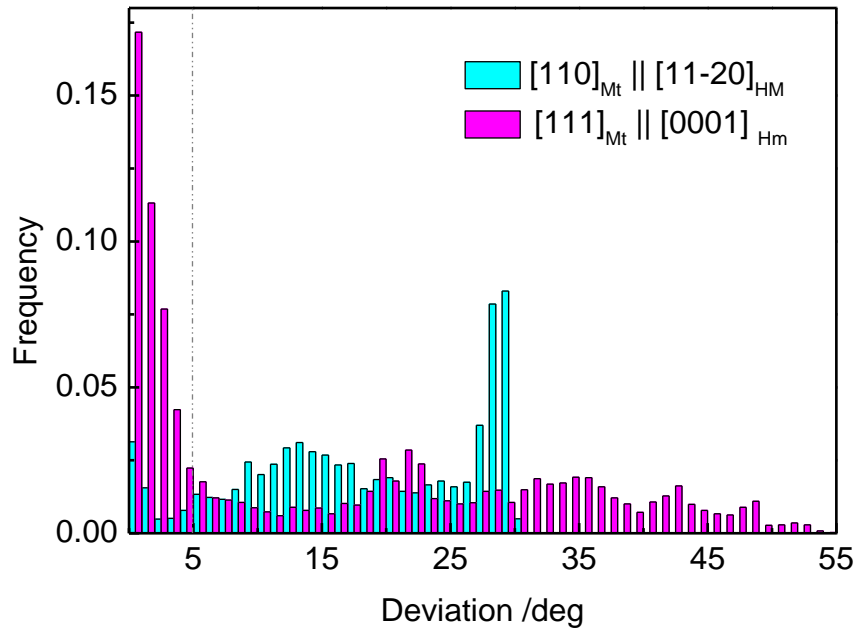


**Fig. 6** Histogram of the lattice correlation boundaries between  $[110]$  of Fe<sub>3</sub>O<sub>4</sub> and  $[11\bar{2}0]$  of  $\alpha$ -Fe<sub>2</sub>O<sub>3</sub>, and  $[111]$  of Fe<sub>3</sub>O<sub>4</sub> and  $[0001]$  of  $\alpha$ -Fe<sub>2</sub>O<sub>3</sub>.

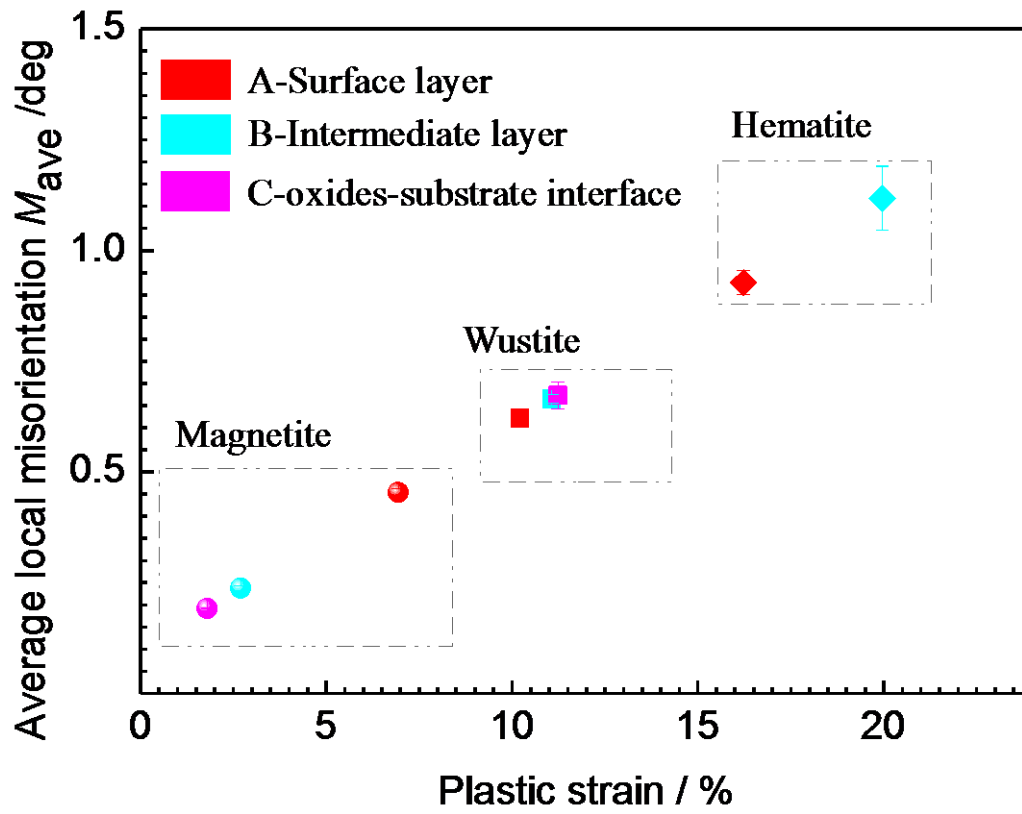


**Fig. 7** Relationship between averaged local misorientation  $M_{ave}$  and macroscopic plastic strain in tertiary oxide scale with different phases.

**Table 1** Chemical compositions of the studied steel.

Elements	C	Si	Mn	P	Cr	S	Al	N	Nb +V+ Ti	Fe
wt.%	0.1	0.15	1.61	0.014	0.21	0.002	0.034	0.003	0.016-0.041	Bal.